REVISION 1

Identifying the spin transition in Fe^{2+}-rich $MgSiO_3$ perovskite from X-ray diffraction and vibrational spectroscopy

Razvan Caracas[1,2,3], Haruka Ozawa[4,5], Kei Hirose,[4,5] Hirofumi Ishii,[6] Nozomu Hiraoka,[6] Yasuo Ohishi,[7] Naohisa Hirao[7]

1) Centre National de la Recherche Scientifique, France
2) Laboratoire de Géologie de Lyon, Université de Lyon, Université Claude-Bernard Lyon 1, Villeurbanne, France
3) Laboratoire de Géologie de Lyon, Ecole Normale Supérieure de Lyon, Site Monod, 15 parvis René Descartes, 69342 Lyon, France
4) Institute for Research on Earth Evolution, Japan Agency for Marine-Earth Science and Technology, Yokosuka, Kanagawa 237-0061, Japan
5) Earth-Life Science Institute, Tokyo Institute of Technology, Meguro, Tokyo 152-8551, Japan
6) National Synchrotron Radiation Research Center, Hsinchu Science Park, Hsinchu 30076, Taiwan
7) Japan Synchrotron radiation Research Institute, Sayo, Hyogo 679-5198, Japan

Abstract

Based on numerical results from density-functional perturbation theory calculations, we show that the magnetic spin transition in Fe^{2+}-rich $MgSiO_3$ perovskite can be identified as changes in the powder X-ray diffraction (XRD) pattern and the vibrational spectra. In particular theory predicts how the symmetry breaking and the volume reduction associated with the spin transition affect both structural and vibrational properties. The XRD measurements of $(Mg_{0.5}Fe_{0.5})SiO_3$ perovskite indeed demonstrated that the new diffraction peaks and the peak broadening formed during the spin transition can be explained by the associated symmetry breaking. We also show computationally that certain vibrational peaks exhibit a shift at the transition;

the Grüneisen parameters of certain modes are affected by the transition, thus bearing on the thermodynamical properties. Raman and/or infrared measurements before and after the spin transition could identify these changes.

Introduction

Fe-bearing perovskite, the major mineral of the Earth's lower mantle, exhibits a magnetic spin transition under compression. The transition corresponds roughly to the reduction of the number of unpaired *d* electrons of Fe^{2+} iron: from 4 unpaired electrons for high-spin state to 0 unpaired electrons for the low-spin state. For Fe^{3+} iron theses numbers decrease from 5 to 3 to 1 unpaired electrons into respectively the high-spin, intermediate-spin and low-spin states. These numbers represent ideal nominal molecular-like values; in a solid there are electronic bands and the magnetic spin is given per unit cell as the difference between the total number of electrons with the two different spins occupying the bands.

The transition depends on a series of factors, like pressure and temperature, iron amount, iron crystallographic site and iron redox state. The ferrous iron on the Mg site stays in high-spin up to large pressures (Bengtson et al. 2009; Hsu et al. 2010a, 2011) when in relatively low, mantle-like concentrations (Bengtson et al. 2008). The ferric iron can be incorporated in both the Mg and the Si sites, with the one on the Si site undergoing a spin transition at very low pressures and the one on the Mg site remaining in high-spin, until the transformation to post-perovskite (e.g., Stackhouse et al., 2007; Irifune et al., 2010; Caracas 2010; Hsu et al. 2011).

The high-spin to low-spin transition of ferrous iron has been documented experimentally with several in situ measurements using nuclear or electronic spectroscopies, like Mössbauer spectroscopy (Jackson et al. 2005; McCammon et al. 2008; Grocholski et al. 2009; Lin et al. 2012) or X-ray emission spectroscopy (XES) (Badro et al. 2004; Li et al. 2004, 2006): a reduction in the local magnetization of the iron atoms is seen either as a change in the Mössbauer pattern or as the disappearance of the Fe $K\beta$ satellite peak in the XES spectra. Several reviews give some very good overlooks of the recent literature on this subject (Hsu et al. 2010b; Lin et al. 2013).

In parallel with the experimental effort, first principles calculations based on density functional theory showed that the transition is associated with a structural distortion corresponding to the reduction in size of the Fe atoms (Umemoto et al.

2010). Such distortion breaks the site symmetry of the iron atoms, allowing a lateral displacement that accommodates the reduction in volume. The electronic changes connected to the magnetic transition have been extensively studied for various iron concentration and configuration in a series of papers (Bengtson et al. 2009; Hsu et al. 2010a; Umemoto et al. 2010). In recent phonon calculations we identified dynamical instabilities in the perovskite structure with orthorhombic symmetry and low-spin configuration. Following the unstable vibrational modes we were able to determine on a strong physical basis the structural distortions and the symmetry breaking associated to the spin transition (Caracas et al. 2011).

The geophysical implications of the spin transition in perovskite are yet a matter of investigation. It was suggested that its effect on the bulk seismic wave velocities is weak, such as at realistic iron concentrations it would not be visible in seismic data (Li et al. 2005). However, the changes in seismic anisotropy, like the ratio of the seismic compressional (Vp) and shear (Vs) wave velocities or the shear wave splitting |Vs1-Vs2|, are sensitive to the spin state of iron. The spin transition can induce differences of anisotropy between the top and the bottom of the lower mantle that are large enough to be visible in seismic data and tomographic studies (Caracas et al. 2010).

The investigations of the effects of the spin transition on the ternary phase diagram of perovskite - post-perovskite – magnesiowüstite and on the iron partitioning between the lower-mantle minerals are still in their incipient phase with no final answer reached so far (Wolf et al. 2008; Metsue and Tsuchiya 2012; Grocholski et al. 2012), but might be important, and one expects important effort to be allocated towards this topics in the near future, from both experiments and calculations. Consequently a rapid and inexpensive method of identification of the spin transition in perovskite is highly desirable.

Because both the electronic and the nuclear spectroscopic methods are rather tedious to perform and require a considerable experimental setup, here we investigate alternate possibilities for identifying the spin transition. We concentrate and discuss only the case of ferrous iron on the A site. We base on the structural distortions and the symmetry breaking that are associated with this spin transition to quantify the potential signature of the transition on X-ray diffraction (XRD) patterns and on vibrational spectra. We show that changes in these spectra would make them viable

methods for identifying the spin transition if careful accurate measurements are recorded.

Methodology

We perform first-principles calculations based on the density functional theory (DFT) in the ABINIT implementation (Gonze et al. 2002, 2009; Torrent et al. 2008).

First we employ the Planar Augmented Wavefunction (PAW) approach to obtain the crystal structures and to investigate the symmetry breaking due to the spin transition. In the PAW method an accurate, all-electron, representation of the electronic system is placed in one-to-one correspondence with a pseudopotential-like treatment of the valence electrons (Blochl 1994). We use the local density approximation (LDA) for the exchange correlation energy. It was shown that the use of more sophisticated exchange correlation formalisms, like the generalized gradient approximation, does not change the physical description of the system, except for an upward shift of the spin transition pressure (Hsu et al. 2010). We adopt 6×6×6 grids of special high-symmetry **k** points (Monkhorst and Pack 1976) to sample the electronic density in the reciprocal space. We employ a 16Ha (1 Ha=27.2116eV) kinetic energy cut-off for the wave functions on the coarse mesh and a 36 Ha cut-off for the wave functions on the finer grid inside the PAW spheres. This set of parameters ensures an accuracy of the calculation better than 1GPa in pressure and 1mHa/unit cell in energy. We fully relax the structures (i.e. we minimize the interatomic force constants and the non-hydrostatic stresses) at several pressures and iron compositions, for both the high-spin and low-spin magnetic configurations. We use the resulting theoretical structures to build the X-ray diffraction pattern, which we compare with experimental patterns.

In a second set of calculations we analyze the lattice dynamical properties of both high-spin and low-spin perovskite within the density-functional perturbation theory (DFPT) (Baroni et al. 2002; Gonze et al. 2005). We use the theoretical structures as determined above in PAW, to determine the phonons in the center of the Brillouin zone. However, because of current implementation restrictions, we do not use PAW for the dynamical calculations, but instead we need to employ Troullier-Martins norm-conserving pseudopotentials. We relax the structures in the standard

norm-conserving formalism, using the same 6×6×6 grids of special high-symmetry **k** points and 40 Ha kinetic energy cutoff.

We compute the low-spin structures of the end-member $FeSiO_3$ term, and then dilute Fe by Mg. Eventually we look at the theoretical X-ray diffraction patterns for $Mg_{0.5}Fe_{0.5}SiO_3$, and at the vibrational pattern of $FeSiO_3$ and $Mg_{0.75}Fe_{0.25}SiO_3$.

Complementary to calculations we obtained in situ X-ray diffraction patterns on powder $Mg_{0.5}Fe_{0.5}SiO_3$ perovskite in a diamond-anvil cell at the BL10XU of SPring-8. Starting material was pyroxene with composition of $Mg_{0.5}Fe_{0.5}SiO_3$ (Tateno et al. 2007). The $Fe^{3+}/\Sigma Fe$ ratio of the starting material was not directly measured but could be ~0.07 according to Sinmyo et al. (2011), in which pyroxene was synthesized in a similar procedure. We compacted the sample powder into pellets and then coated the surface of the sample with gold on both sides, which served as a laser absorber. This coating technique reduces temperature gradients, and thus minimizes chemical heterogeneity caused by Soret diffusion (Sinmyo and Hirose 2010). It was loaded into a hole in a pre-indented rhenium gasket, together with thermal insulation layers of dried NaCl. The assembly was compressed by beveled diamond anvils with 150 μm culet. Angle-dispersive XRD patterns were collected on an imaging plate. A monochromatic incident X-ray beam with a wavelength of 0.41351 Å was collimated to about 6-μm area (full-width of half maximum) on the sample. Two-dimensional XRD images were integrated as a function of two-theta angle in order to have a conventional one-dimensional diffraction profile using the IPAnalyzer (Seto et al. 2010). The sample was heated by a couple of fiber lasers using the double-sided heating technique. Temperature was measured by fitting the thermal radiation spectrum to the Planck radiation function using the spectro-radiometric method (Ohishi et al. 2008). Pressure was determined from the unit-cell volume of gold, using the equation of state proposed by Tsuchiya (2003). Pressure uncertainty arising from the uncertainty in unit-cell volume was ±0.6 GPa.

We also recorded several X-ray emission spectra on samples undergoing the spin transition. XES is an established technique widely used to study high-spin to low-spin crossover in transition-metal elements and their compounds. For samples containing iron in a high-spin state, the emission spectra consist of $K\beta_{1,3}$ main peak at 7058 eV and satellite $K\beta'$ peak located at lower energy appearing as a result of the exchange interaction between 3*p* core-hole and 3*d* in a final state of the emission process. The iron spin crossover results in a loss of 3*d* magnetic moment, leading to a

disappearance of such satellite peak. High-resolution X-ray emission spectra of the Fe *Kβ* line were obtained for $Mg_{0.5}Fe_{0.5}SiO_3$ perovskite at the BL12XU beamline of SPring-8 (Ozawa et al. 2011). Such measurements were carried out at room temperature in a DAC at pressures between ambient pressure and 100 GPa (run #2), and 93 and 98 GPa (run #3). We used beveled anvils with 200 μm culet. Starting material was prepared by heating $Mg_{0.5}Fe_{0.5}SiO_3$ gel to 1273 K under the oxygen fugacity slightly above the iron-wüstite buffer in run #2. In run #3, the pyroxene starting material same as that in run #1 was used. The gel starting material may have higher $Fe^{3+}/\Sigma Fe$ ratio of ~0.2 according to Ohta et al. (2008). The sample coated with gold was loaded together with thermal insulation layers of dried NaCl, into an X-ray translucent gasket that was composed of cubic boron nitride and beryllium. Such composite gasket can increase the thickness of the sample chamber and reduce the contribution from iron impurity in beryllium. The sample was compressed to high pressure at 300 K and then heated by laser from both sides with scanning the laser beam. The high-pressure phase was subsequently identified by XRD measurements at BL10XU. Pressure was determined at room temperature based on the Raman shift of the T_{2g} mode of the culet of diamond anvil (Akahama and Kawamura 2004). We used monochromatic X-rays at 11 keV as an incident beam for XES measurements. It was collimated to ~15 μm in diameter at the sample. The pressure variations within the area from which XES spectra were collected were less than 3 GPa. A 1m Rowland circle type spectrometer, equipped with 1m spherical bent Ge (620) analyzer, was used to acquire the emission spectra. These spectra were collected through the gasket in order to avoid a loss of intensity due to absorption by the diamond. The spectra covered the energy range from 7020 to 7080 eV with a resolution of 0.8 eV.

Results

Structural implications of the spin transition

In recent lattice dynamical calculations we showed that $FeSiO_3$ perovskite, with orthorhombic *Pbnm* symmetry, in both the intermediate spin and the low spin state exhibits unstable phonon modes (Caracas et al. 2011). These instabilities correspond to displacements of the Fe sub-lattice accompanied by a rearrangement of

parts of the O sub-lattice. The spin transition is also accompanied by a density difference of 4.9% at 20 GPa going down quasi-linearly to 3.8% at 120 GPa. Based on the two $MgSiO_3$ and $FeSiO_3$ end-members we are now able to construct the correct guess structures for the intermediate compositions along the Mg-Fe join in both high-spin and in low-spin magnetic configurations. Then using these initial geometries the appropriate structural relaxation eventually yields the correct final structures. For the high-spin case, the orthorhombic symmetry is preserved along the whole Mg-Fe join. The local replacement pattern of the two cations breaks the local symmetry in specific configurations, but the large-scale average structure remains orthorhombic. The starting geometry can be obtained by replacing Mg with Fe in the $MgSiO_3$ structure or Fe with Mg in the $FeSiO_3$ structure, the final result being the same. For the low-spin case the structure exhibits distortions that lower its symmetry down to monoclinic or triclinic even for the pure $FeSiO_3$ end-member term. Actually, in order to be able to preserve these distortions, and prevent the code from finding a local minimum, along the solid solution, we need to start with the distorted low-spin structure of $FeSiO_3$ and replace Fe with Mg in the desired amount. Indeed, starting the simulations from orthorhombic $FeSiO_3$ fails to find the appropriate global minimum and the correct low-spin crystal structures (Bengtson et al. 2009; Hsu et al. 2010a; Umemoto et al. 2010, Caracas et al., 2011).

The spin transition has thus two different structural facets: symmetry breaking and volume reduction. The correlation between the spin transition and the distortions of the orthorhombic structure should be reflected in changes of the symmetry of certain physical properties, like the Raman and infrared spectra or the XRD patterns. These changes could be observed as possible appearances of new peaks and/or broadening of the existent ones. The volume and interatomic bond distance reductions associated with the spin transition should be reflected in shifts of the positions of the peaks in vibrational spectra and in the XRD patterns. Accurate in situ Raman/infrared and XRD measurements could then capture at least some of these features. Here we analyze these different changes and illustrate them for several particular terms along the solid solution.

X-ray powder diffraction pattern

Figures 1a and 1b show calculated X-ray diffraction patterns of the theoretical structure of the middle term of the solid solution, $Mg_{0.50}Fe_{0.50}SiO_3$, in respectively high-spin and low-spin configurations, computed at 90 GPa. We use one unit cell with 4 formula units, i.e. 4 A sites, where we replace half the A atoms with Mg and half with Fe. Basic math tells us there are six possibilities, i.e. combinations of four by two. In the high-spin phases, there are no distortions associated to the spin, the orthorhombic symmetry is preserved (even though some forbidden reflections conditions might be lifted), which makes the four crystallographic sites equivalent. When we proceed with the Fe/Mg replacements, based on symmetry-determined multiplicities, only three different Fe/Mg atomic configurations are needed to describe the high-spin state. In the low-spin phase, there are distortions associated to the spin, the orthorhombic symmetry is not preserved, and the four A sites are not equivalent anymore. Eventually six configurations are needed to describe all possible Mg/Fe distribution in one unit cell for the low-spin state.

For the high-spin magnetic cases we choose the ferromagnetic configuration, as the structural differences between the ferromagnetic and the antiferromagnetic orthorhombic $FeSiO_3$ are small enough not to be detectable in diffraction. Arrows in panel *b* show the changes occurring due to the spin transition, like broadening of the peaks and appearance of new weaker peaks and shoulders.

In a powder experiment of a solid solution crystal, each configuration would contribute with its own diffraction pattern, to both peak position and intensities. For our case, though within a limited configurational space, we may distinguish between several such different atomic arrangements. The corresponding diffraction of each one of them is represented with light red lines in Figures 1a and 1b. They are then summed up to obtain the full powder diffraction spectrum, represented by the bold blue lines.

All the major diffraction peaks preserve their position and intensity throughout the spin transition. But the spectra before and after the transition are different in the detail, as shown in Figures 1a and b due to symmetry breaking. Several new peaks appear in the low-spin phase as a result of degeneracy lifting, and new shoulders develop and grow to result in somewhat broader peaks than in the case of the high-spin spectrum. This is due to the degeneracy lifting for the structural configurations. In this way more individual contributions are recorded, and almost each one is but slightly different from the others. This symmetry breaking lifts degeneracies between

diffraction peaks like the orthorhombic 110 and -110. They are the same in an orthorhombic group, but different in a monoclinic or triclinic group occurring after the spin transition. In the latter symmetry setup, this would result in two peaks. If the non-orthorhombic distortions are small then they can overlap or appear as shoulders and/or broadening of the same larger peak. Their intensity can increase too, as is the case for the -110 peak at 7.4° 2θ angle and the 102 and 012 peaks above 9° 2θ angles. The latter sets of peaks are invisible in MgSiO3 perovskite, become very weakly visible in the high-spin configuration because of the Mg/Fe substitution that lifts the ban of this phase extinction, and have their intensity enhanced in the low-spin phase because of the symmetry breaking and associated structural distortions.

Similarly, a set of new weak peaks appears due to lifting and changing the selection rules as a result the symmetry breaking. For example the orthorhombic space group bans a series of reflections, like h00, 0k0, or 00l with h, k, or l even numbers or the 0kl with l odd, namely peaks like 012, 102, etc. (Hahn and Arroyo 2006). Any distortion would then break at least some of these rules. Again, if the distortion is small, the resulting new peaks are weak, but visible, and would occur after the spin transition. Such peaks are the 02-1 around 11.5° 2θ angles, the 02-2 around 13° 2θ angles, and the 123 around 15.9° 2θ angles. They are all represented with arrows in Figure 1b, and they all have their correspondence in both experiment and theory.

The experimental XRD pattern, recorded at 89 GPa and 300 K after heating at around 2000 K for 1 hour is represented in Figure 1c. Both theoretical and experimental patterns use 0.414 Å wavelength radiation. Refined experimental lattice parameters are a=4.4395±0.0038 Å; b=4.6361±0.0027 Å; c=6.4144±0.0069 Å; V=132.02±0.20 Å^3. These values are within 1% of the theoretical, which are respectively 4.42 Å, 4.64 Å, and 6.39 Å at 90 GPa. Consequently, the exact position and intensity of the diffraction peaks are only slightly different between the theoretical and the experimental structures because of these differences in pressure/volume, and because of the precise iron amount and iron distribution. In order to further decrease these discrepancies for our comparison, we use the experimental lattice parameters to model the theoretical spectra in Figure 1a and 1b.

Apart from intensity rescaling, there is an excellent one-to-one correlation between all the major peaks of the theoretical and the experimental patterns. All these

major peaks can be indexed using the orthorhombic setting. Stars in panel c denote several weak peaks that cannot be indexed using the orthorhombic setting. This may suggest that something happened to the structure, which affected the details of the atomic arrangements, but not the general topology. At least two, possibly four, of these peaks have a good match to the new theoretical peaks predicted to occur during the spin transition. It is possible that the remaining unindexed peaks correspond to particular Mg/Fe configurations that were not explicitly covered in our theoretical analysis.

Finally we perform additional XES measurements (runs #2 and 3) to examine the spin state of iron in $Mg_{0.5}Fe_{0.5}SiO_3$ perovskite. In the first set of experiments, the sample was squeezed to 93 GPa at room temperature. The sample was then heated at 1700-2100K for 43 minutes and the diffraction peaks from the perovskite phase appeared upon heating. Subsequently, the spin state was examined by XES at 88 GPa and 300 K. Next we increased the pressure to 100 GPa and obtained the X-ray emission spectrum. Afterwards, the spectra were collected with decreasing pressure down to ambient pressure. In the second run, we first compressed the sample to 93 GPa. During subsequent heating at 2000-2300 K, the peaks of perovskite appeared. After heating for 110 mins, the X-ray emission spectrum was obtained at 93 GPa and room temperature. Next we increased the pressure and collected the spectrum at 98 GPa.

Vibrational spectra

A second set of alternative methods proposed here for the identification of the spin transition is represented by the vibrational spectroscopies, like Raman or infrared. The volume collapse at the transition induces a hardening of the phonons visible as an upward shift of all modes at the transition. Furthermore, the symmetry breaking participates to changing the Grüneisen parameters and also may induce changes of the mode characters, which in turn can be reflected in their activation for either Raman or infrared spectroscopy.

Figure 2 shows the correspondence of the theoretical vibration modes in the zone-center between the high-spin and the low-spin phases. The calculations were done for the pure $FeSiO_3$ end-member term and for one configuration of the intermediate term $(Mg_{0.75}Fe_{0.25})SiO_3$. The frequencies of the modes in the low-spin

phases are represented on the horizontal axes and in the high-spin phase on the vertical axes. If there were no changes at the spin transition, all the points would fall on the black diagonal line. The spread and the negative shift of modes in the high-spin with respect to the low-spin, suggest changes occur at the transition. These changes are strong for the pure end-member term (panel a), but changes in specific peaks could be visible even for large dilutions (panel b), with only 25% Fe on the Mg site.

For the end-member $FeSiO_3$ term, represented in Figure 2a there is a clear shift of the majority of the phonon frequencies at the spin transition, e.g. a mode at 400 cm^{-1} in the high-spin phase is found in the low-spin not at 400 cm^{-1} (this would fall on the black line), but above. This shift can actually be as large as 150 cm^{-1} or more for some specific modes, notably the low-frequency modes dominated by the displacements of the iron atoms. The shift in the higher-frequency modes, dominated by O displacements is due to the modifications in the geometry and bond distances within the Fe-O coordination polyhedral. The last highest-frequency modes are only weakly affected by the spin transition as these modes are dominated by the breathing modes of the octahedra, which do not suffer much from the magnetic collapse.

The same pattern is observed even for diluted systems, along the $MgSiO_3$-$FeSiO_3$ join. Figure 2b shows the shifts for a composition of 75%Mg and 25%Fe, not far from realistic iron concentrations. Even here the frequencies of the phonon modes exhibit a raise in wavevector number. The most significant changes are for the modes whose eigenvectors are dominated by the displacements of the iron atoms; in these cases the upward shifts can reach almost 100 cm^{-1}.

The inset in Figure 2(b) shows the pressure dependence of the frequencies for several modes, whose derivatives yield the Grüneisen parameters, clearly different between the high-spin and the low-spin phases.

Discussion

The occurrence of the spin transition for an intermediate term in a solid solution, like $MgSiO_3$-$FeSiO_3$, is a continuous process over a certain pressure (and temperature) range (Tsuchiya et al. 2006). Consequently, the peak shifts of both diffraction and vibrational patterns associated to the volume collapse due to the spin transition are smoothed out; then one would not expect to be able to detect them.

Similarly, other changes of the diffraction, like appearance of new peaks, broadening of others, etc., are not sudden but continuous and would be hard to follow experimentally. However differences should occur in the patterns before and after the transition, i.e. between the high-spin and the low-spin phases, in terms of general topology and/or pressure dependence.

The smoothness of such a transition is clearly observed in the experimentally obtained X-ray emission spectra. The relatively low-pressure range of spin transition of ferrous iron in Fe-rich perovskite is consistent with theoretical predictions (Bengtson et al. 2008; Umemoto et al. 2008). Figure 3 shows such a spectrum recorded in situ for pressures up to 100 GPa. The thermodynamic path was mostly decompression. A satellite *Kβ*' peak is clearly observed occurring with decreasing pressure, a mark for the presence of a high-spin state at low pressures. At higher pressure the peak does not vanish completely, when compared to the FeO low-spin reference. This suggests either a non-complete spin transition, or a possibility of some residual Fe^{3+} contributing to the electronic density.

Finally the smoothness of the transition would make any shift in Raman or infrared frequencies hardly visible in an experimental measurement. However, as shown in the inset of Figure 2b, the pressure derivatives, i.e. the Grüneisen parameters, of some particular modes are different in the high-spin and the low-spin phases. This would make them preferred tracers of the spin transition: the Grüneisen parameters of these modes would have two distinct values at low and high pressures with an average intermediate trend as the transition advances.

Implications

We have shown that the spin transition of iron in Fe^{2+}-bearing $MgSiO_3$ perovskite bears specific signatures in both XRD patterns and Raman/infrared spectra. Our assertions are based on results from first-principles calculations performed within the density-functional theory. The volume collapse and the symmetry breaking associated to this transition make that new peaks may appear in diffraction. Experimental recordings of powder diffraction data on iron-rich perovskite samples after the spin transition support our numerical results.

However, caution must be paid, because the relative low intensity of these extra peaks makes them hard to observe in more Fe-diluted systems. Already for the large Fe concentrations of our samples, the strong NaCl and Au reflections together with a high background, make the observation and identification of such peaks a difficult task (hence both solid and dashed arrows in Figure 1c). For example recent single-crystal experimental data (Boffa Ballaran et al. 2012) on diluted samples (4 mol % Fe) did not observe the distortions seen here. Moreover some of the theoretical peaks overlap with the reflections of Au, and thus cannot be observed experimentally.

Certain Raman and infrared modes exhibit an upward frequency shift during the transition, and different Grüneisen parameters in the high-spin and the low-spin phases. While this still waits for experimental confirmation, the predicted changes in Grüneisen parameters could signify differences in the thermodynamical properties of perovskite before and after the spin transition, differences not only due to volume, but intrinsic to the structure.

This can have further implications for modeling the Earth's mantle, if such a transition takes place at large depths. But even if the transition in perovskite occurs beyond the thermodynamical limits of the Earth's mantle, our study suggests that more attention should be paid to the effect of the spin transition on physical properties of mantle minerals other than seismic.

Acknowledgements

Calculations have been performed on the JADE machine of CINES (Centre Informatique National de l'Enseignement Supérieur, Montpellier, France) under DARI grant x2013106368, and on the machines of the PSMN (Pole de Simulation et Modélisation Numérique, Ecole Normale Supérieure de Lyon). RC acknowledges financial support from INSU of CNRS. We thank K. Fujino and S. Tateno for technical support on XES measurements. The synchrotron XRD experiments were conducted at BL10XU of SPring-8 (Proposal No. 2011B0087 and 2012B0087), and XES experiments were performed at BL12XU with the approval of JASRI/SPring-8 and NSRRC, Taiwan (2011B4258/20XX-X-XXX-X).

Bibliography

Akahama, Y., Kawamura, H. (2004), High-pressure Raman spectroscopy of diamond anvils to 250 GPa: Method for pressure determination in the multimegabar pressure range, Journal of Applied Physics, 96, 3748-3751.

Badro, J., Rueff, J. P., Vankó, G., Monaco, G., Fiquet, G., and Guyot, F. (2004), Electronic transitions in perovskite: Possible nonconvecting layers in the lower mantle, Science, 305, 383–386.

Baroni, S., de Gironcoli, S., Dal Corso, A., and Giannozzi, P. (2001) Phonons and related crystal properties from density-functional perturbation theory. Reviews in Modern Physics, 73, 515–562.

Bengtson, A., Persson, K., and Morgan, D. (2008), Ab initio study of the composition dependence of the pressure induced spin cross-over in perovskite $(Mg_{1\_x},Fe_x)SiO_3$, Earth and Planetary Science Letters, 265, 535–545.

Bengtson, A., Li, J., and Morgan, D. (2009), Mössbauer modeling to interpret the spin state of iron in $(Mg,Fe)SiO_3$ perovskite, Geophysical Research Letters, 36, L15301, doi:10.1029/2009GL038340.

Blochl, P.E. (1994), Projector augmented-wave method. Physical Review B, 50, 17953-17979.

Boffa Ballaran, T., Kurnosov, A., Glazyrin, K., Frost, D. J., Merlini, M., Hanfland, M., and Caracas, R. (2012) Effect of chemistry on the compressibility of silicate perovskite in the lower mantle. Earth and Planetary Science Letters 333–334, 181–190.

Caracas, R. (2010), Spin and structural transitions in $AlFeO_3$ and $FeAlO_3$ perovskite and post-perovskite, Physics of the Earth and Planetary Interiors, 182, 10-17.

Caracas, R. and Cohen, R.E. (2005), Effect of the chemistry of the stability and elasticity of the perovskite and post-perovskite phases in the $MgSiO_3$-$FeSiO_3$-Al_2O_3 system and implications for the lowermost mantle, Geophysical Research Letters, 32, L16310, doi:10.1029/2005GL023164, 2005a.

Caracas, R., and Cohen, R.E. (2007), Effect of chemistry on the physical properties of perovskite and post-perovskite, in Post-Perovskite: The Last Mantle Phase Transition, Geophysical Monogaphy. Series 174, doi:10.1029/174GM10.

Caracas, R., and Cohen, R.E. (2008), Ferrous iron in post-perovskite from first-principles calculations, Physics of the Earth and Planetary Interiors, 168, 147-152.

Caracas, R., Mainprice, D., and Thomas, T. (2010) Is the spin transition in Fe^{2+}-bearing perovskite visible in seismology? Geophysical Research Letters, 37, L13309, doi:10.1029/2010GL043320

Caracas, R., Ozawa, H., and Hirose, K. (2011) Identification of the Spin Transition in Fe-bearing Perovskite and Implications for the Lower Mantle, Abstract MR34A-08, presented at 2011 Fall Meeting AGU.

Gonze, X., Beuken, J.-M., Caracas, R., Detraux, F., Fuchs, M., Rignanese, G.-M., Sindic, L., Verstraete, M., Zerah, G., Jollet, F., Torrent, M., Roy, A., Mikami, M., Ghosez, Ph., Raty, J.-Y., and Allan, D. C. (2002) First-principle computation of material properties the ABINIT software project. Computational Materials Science, 25, 478–492. [http//www.abinit.org]

Gonze, X., Rignanese, G.-M., and Caracas, R. (2005) First-principles studies of the lattice dynamics of crystals, and related properties. Zeitschrift für Kristallographie, 220, 458–472.

Gonze, X., Amadon, B., Anglade, P.-M., Beuken, J.-M., Bottin, F., Boulanger, P., Bruneval, F., Caliste, D., Caracas, R., Côté, M., Deutsch, T., Genovesi, L., Ghosez, Ph., Giantomassi, M., Goedecker, S., Hamann, D.R., Hermet, P., Jollet, F., Jomard, G., Leroux, S., Mancini, M., Mazevet, S., Oliveira, M.J.T., Onida, G., Pouillon, Y., Rangel, T., Rignanese, G.-M., Sangalli, D., Shaltaf, R., Torrent, M., Verstraete, M.J., Zerah G., and Zwanziger, J.W. (2009) ABINIT: First-principles approach to material and nanosystem properties. Computer Physics Communications, 180, 2582-2615.

Grocholski, B., Catalli, K., Shim, S. H., and Prakapenka, V. (2012) Mineralogical effects on the detectability of the post-perovskite boundary. Proceedings of the National Academy of Science U.S.A., 109, 2275-2279.

Grocholski, B., Shim, S. H., Sturhahn, W., Zhao, J., Xiao, Y., and Chow, C. (2009), Spin and valence states of iron in $(Mg_{0.8}Fe_{0.2})SiO_3$ perovskite, Geophysical Research Letters, 36, L24303, doi:10.1029/ 2009GL041262.

Hahn, Th., and Arroyo, M. I. (2006) *International Tables for Crystallography* (2006). Volume A, *Space-group symmetry, International Union of Crystallography*.

Hirose, K., Takafuji, N., Fujino, K., Shieh, S. R., and Duffy, T. S. (2008), Iron partitioning between perovskite and post- perovskite: A transmission electron microscope study, American Mineralogist, 93, 1678–1681.

Hsu H., Umemoto, K., Blaha, P., and Wentzcovitch, R. (2010a), Spin states and hyperfine interactions of iron in $(Mg,Fe)SiO_3$ perovskite under pressure. Earth and Planetary Science Letters, 294,19-26.

Hsu, H., Umemoto K., Wu, Z., and Wentzcovitch, R. M. (2010b), Spin-State Crossover of Iron in Lower-Mantle Minerals: Results of DFT+U Investigations, Reviews in Mineralogy and Geochemistry, 71, 169-199.

Hsu, H., Blaha, P., Cococcioni, M., and Wentzcovitch, R. M. (2011), Spin-state crossover and hyperfine interactions of ferric iron in $MgSiO_3$ perovskite, Physical Review Letters, 106, 118501.

Irifune, T., Shinmei T., McCammon, C., Miyajima, N., Rubie, D. C., and Frost, D. J. (2010) Iron Partitioning and Density Changes of Pyrolite in Earth's Lower Mantle, Science, 327, 193-195.

Jackson, J. M., Sturhahn, W., Shen, G., Zhao, J., Hu, M.Y., Errandonea, D., Bass, J. D., and Fei, Y. (2005), A synchrotron Mössbauer spectroscopy study of $(Mg,Fe)SiO_3$ perovskite up to 120 GPa, American Mineralogist, 90, 199–205.

Li, J., Struzhkin, V. V., Mao, H. K., Shu, J., Hemley, R. J., Fei, Y., Mysen, B., Dera, P., Prakapenka, V., and Shen, G. (2004), Electronic spin state of iron in lower mantle perovskite, Proceedings of the National Academy of Science U.S.A., 101, 14027–14030.

Li, J., Sturhahn, W., Jackson, J. M., Struzhkin, V. V., Lin, J. F., Zhao, J., Mao, H. K., and Shen, G. (2006), Pressure effect on the electronic structure of iron in $(Mg,Fe)(Si,Al)O_3$ perovskite: A combined synchrotron Mössbauer and X-ray emission spectroscopy study up to 100 GPa, Physics and Chemistry of Minerals, 33, 575–585.

Li, L., J. P. Brodholt, S. Stackhouse, D. J. Weidner, M. Alfredsson, and G. D. Price (2005b), Elasticity of $(Mg,Fe)(Si,Al)O_3$-perovskite at high pressure, Earth and Planetary Science Letters, 240, 529–536.

Lin, J. F., Alp, E. E. Mao, Z. Inoue, T. McCammon, C. Xiao, Y. Chow, P. and Zhao J. (2012), Electronic spin and valence states of iron in the lower-mantle silicate perovskite by synchrotron Mössbauer spectroscopy, American Mineralogist, 97, 592–597.

Lin, J. F., Speziale, S., Mao, Z., and Marquardt, H. (2013) Effects of the electronic spin transitions of iron in lower mantle minerals: Implications for deep mantle geophysics and geochemistry, Reviews in Geophysics, 51, doi:10.1002/rog.20010.

Mao, W.L., Meng, Y., Shen, G., Prakapenka, V.B., Campbell, A. J., Heinz, D. L., Shu, J., Caracas, R., Cohen, R.E., Fei, Y., Hemley R. J., and Mao, H.-k. (2005),

Iron-rich silicates in the Earth's D" layer. Proceedings of the National Academy of Science, 102, 9751-9753.

McCammon, C., Kantor, I., Narygina, O., Rouquette, J., Ponkratz, U., Sergueev, I., Mezouar, M., Prakapenka, V. B., and Dubrovinsky, L. (2008), Stable intermediate-spin ferrous iron in lower mantle perovskite, Nature Geoscience, 1, 684–687.

McCammon, C., Dubrovinsky, L., Narygina, O., Kantor, I., Wu, X., Glazyrin, K., Sergueev, I., and Chumakov, A. I. (2010), Low-spin Fe^{2+} in silicate perovskite and a possible layer at the base of the lower mantle, Physics of the Earth and Planetary Interiors, 180, 215–221.

Metsue, A., and Tsuchiya, T. (2012), Thermodynamic properties of $(Mg,Fe^{2+})SiO_3$ perovskite at the lower-mantle pressures and temperatures: An internally consistent LSDA + U study, Geophysical Journal International, 190, 310–322.

Monkhorst, H. J., and Pack, J. D. (1976), Special points for Brillouin-zone integrations. Physical Review B, 13, 5188-5192.

Ohishi, Y., Hirao, N., Sata, N., Hirose, K., and Takata, M. (2008), Highly intense monochromatic X-ray diffraction facility for high-pressure research at SPring-8, High Pressure Research, 28, 163-173.

Ozawa, H., Hirose, K., Ohta, K., Ishii, H., Hiraoka, N., Ohishi, Y., Seto, Y. (2011), Spin crossover, structural change, and metallization in NiAs-type FeO at high pressure, Physical Review B, 84, 134417.

Seto, Y., Nishio-Hamane, D., Nagai, T., and Sata, N. (2010), Development of a software suite on X-ray diffraction experiments, The Review of High Pressure Science and Technology, 20, 269-276.

Sinmyo, R., and Hirose, K. (2010), The Soret diffusion in laser-heated diamond-anvil cell, Physics of the Earth and Planetary Interiors, 180, 172-178.

Stackhouse, S., Brodholt, J. P., and Price, D, G. (2007), Electronic spin transitions in iron-bearing $MgSiO_3$ perovskite, Earth and Planetary Science Letters, 253, 282-290.

Tateno, S., Hirose, K., Sata, N., and Ohishi, Y. (2007), Solubility of FeO in $(Mg,Fe)SiO_3$ perovskite and the post-perovskite phase transition, Physics of the Earth and Planetary Interiors, 160, 319-325.

Torrent, M., Jollet, F., Bottin, F., Zerah G., and Gonze, X. (2008), Implementation of the projector augmented-wave method in the ABINIT code: Application to the study of iron under pressure, Computational Material Science, 42, 337-351.

Tsuchiya, T. (2003), First-principles prediction of *P-V-T* equation of state of gold and the 660-km discontinuity in Earth's mantle, Journal of Geophysical Research, 108, 2462, DOI:10.1029/2003JB002446.

Tsuchiya, T., Wentzcovitch, R. M., da Silva, C. R. S., de Gironcoli, S. (2006) Spin transition in magnesiowuestite in Earth's lower mantle. Physical Review Letters 96, 198501.

Umemoto, K., Wentzcovitch, R. M., Yu, Y. G., and Requist, R. (2008), Spin transition in (Mg,Fe)SiO_3 perovskite under pressure, Earth and Planetary Science Letters, 276, 198–206.

Umemoto, K., Hsu, H. and Wentzcovitch, R. M. (2010), Effect of site degeneracies on the spin crossovers in (Mg, Fe)SiO_3 perovskite, Physics of the Earth and Planetary Interiors 180, 209–214.

Wolf, A. S., Caracas, R., and Asimow, P.D. (2008) Thermodynamic Phase Relations in the MgO-FeO-SiO_2 System in the Lower Mantle, Eos Trans. AGU, 89(53), Fall Meet. Suppl., Abstract MR42a-03.

Figure 1. Theoretical X-ray diffraction patterns for the $(Mg_{0.5}Fe_{0.5})SiO_3$ perovskite in high- (a) and low- (b) spin configurations. The symmetry breaking that is associated to the spin transition induces changes in the diffraction pattern, like appearance of new peaks, shoulders and peak broadening. Red arrows in (b) point to such new peaks. (c) Room-temperature XRD patterns of $Mg_{0.5}Fe_{0.5}SiO_3$ collected after heating at 89 GPa. The diffraction peaks from $Mg_{0.5}Fe_{0.5}SiO_3$ perovskite were indexed on an orthorhombic *Pbnm* cell. Pv, perovskite; Au, gold. In situ experimental diffraction patterns show clearly the occurrence of such new peaks after the spin transition. Red arrows in (c) point to the correspondence between the new diffraction peaks predicted by calculations and the experimental peaks, which cannot be indexed using a standard orthorhombic structure for perovskite: solid and dashed lines correspond to certain and less certain correspondence. Theoretical diffraction patterns are obtained using the experimental lattice parameters, and theoretical reduced atomic positions, to account for the symmetry breaking. This minimizes the peak position mismatch due to the standard discrepancies between DFT and experimental volumes and pressures.

Figure 2. Correspondence between the theoretical frequencies of the vibrational mode in zone center for pure $FeSiO_3$ perovskite (a) and for $(Mg_{0.75}Fe_{0.25})SiO_3$ perovskite (b), computed at several pressures. The frequencies in the low-spin are on the horizontal axis and in the high-spin are on the vertical axis. If there were no changes due to the spin transition all the points would fall on the black lines, which is clearly not the case. The inset in panel (b) shows the pressure (horizontal axis in GPa) dependence of the frequencies (vertical axis in wavenumbers in cm^{-1}) of several modes in both the high-spin (solid line) and the low-spin (dashed line) phases. Their derivatives, i.e. the Grüneisen parameters, are clearly different between the two spin states.

Figure 3. (a) Evolution of X-ray emission spectra of $Mg_{0.5}Fe_{0.5}SiO_3$ perovskite (solid squares, run #2; open squares, run #3). Measurements were conducted at 300 K. All spectra are normalized to transmitted intensity, and shifted so that the weighted average of main ($K\beta$) plus satellite ($K\beta$') emission lines is set to 7058 eV. X-ray emission spectrum of FeO at 146 GPa is also shown as a reference of Fe^{2+} in low-spin state (Ozawa et al. 2011). (b) Normalized intensity of the $K\beta$' peak as a function of

623 pressure; same symbols as (a). The intensity of the satellite peak was obtained by
624 subtracting each spectrum from the reference spectrum shown in (a). The intensity of
625 the *Kβ*' peak is proportional to the relative abundance of the high-spin and low-spin
626 species (Badro et al. 2004). The intensity of the satellite Fe *Kβ* peak clearly
627 diminishes with pressure, but fails to disappear completely, suggesting that some
628 residual iron did not yet undergo the spin transition.

a)

HS

b)

LS

Exp.

Pv 110 + 002
Pv 111
NaCl 100
Pv 020
Pv 112
Pv 200
Au 111
NaCl 110
Pv 211
Au 200
Pv 202
Pv 113
Pv 122
Pv 212
+ 004
Pv 023
Pv 221
Pv 130
Pv 222
Pv 131
NaCl 200
Au 220
NaCl 111 Pv 220 + 0

89 GPa, 300 K

C)

Intensity

Azimuthal angle (deg.)

2-theta angle (deg.)

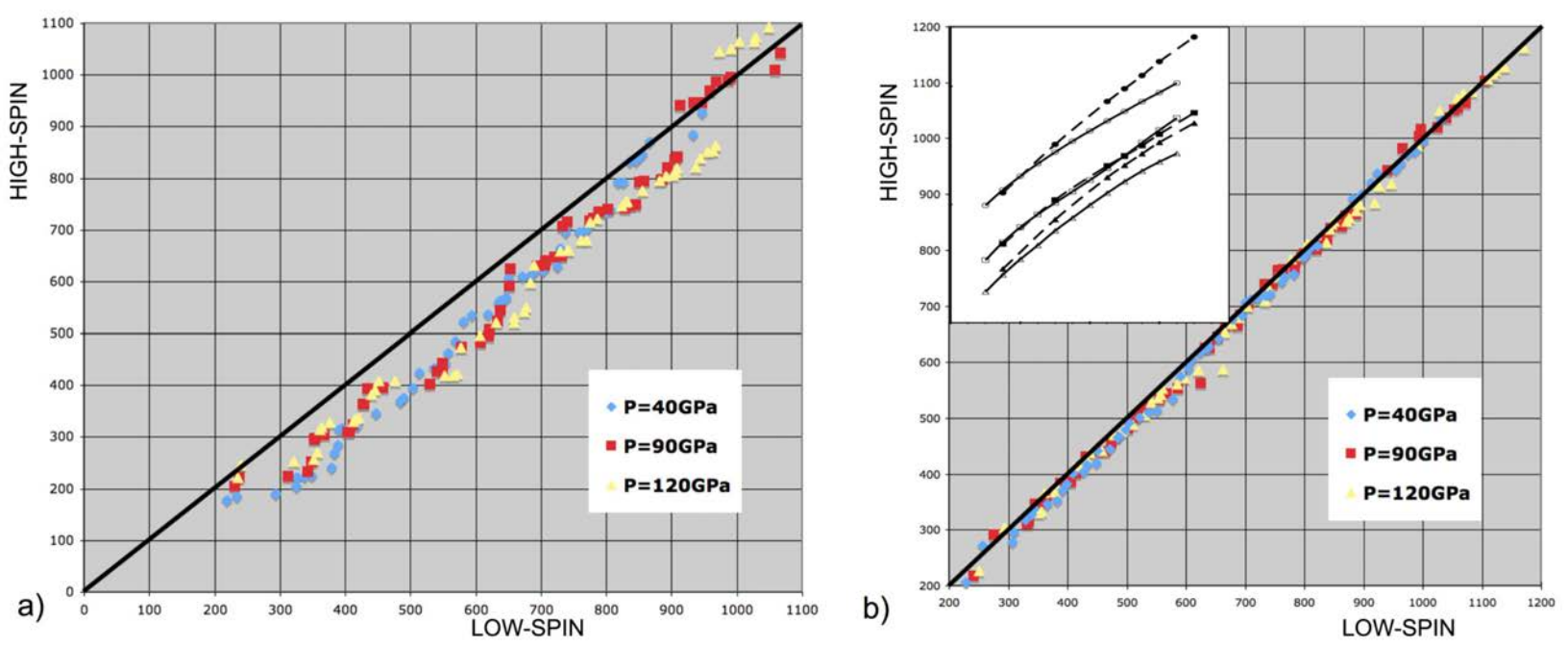
HIGH-SPIN
LOW-SPIN
P=40GPa
P=90GPa
P=120GPa
a)
b)

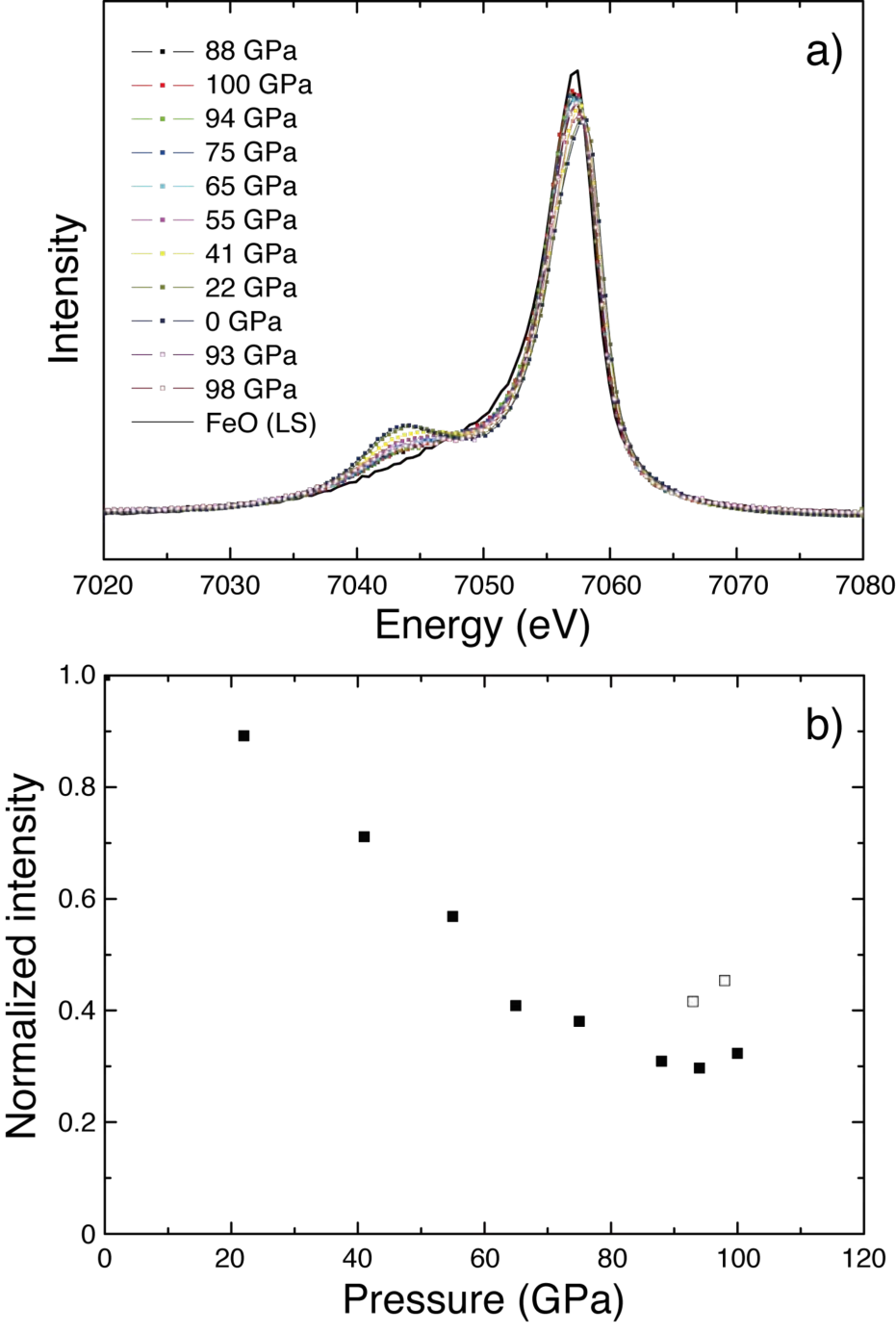
a)
88 GPa
100 GPa
94 GPa
75 GPa
65 GPa
55 GPa
41 GPa
22 GPa
0 GPa
93 GPa
98 GPa
FeO (LS)
Intensity
7020
7030
7040
7050
7060
7070
7080
Energy (eV)
b)
Normalized intensity
1.0
0.8
0.6
0.4
0.2
0
0
20
40
60
80
100
120
Pressure (GPa)